Science Bulletin 64 (2019) 1881–1889

Contents lists available at ScienceDirect

Science Bulletin

journal homepage: www.elsevier.com/locate/scib

Science Bulletin
www.scibull.com

Article

Photochemical cycloaddition and temperature-dependent breathing in pillared-layer metal–organic frameworks

Qingqing Pang, Binbin Tu, Lingyi Yang, Qiaowei Li *

Department of Chemistry, Collaborative Innovation Center of Chemistry for Energy Materials (iChEM), and Shanghai Key Laboratory of Molecular Catalysis and Innovative Materials, Fudan University, Shanghai 200438, China

ARTICLE INFO

Article history:
Received 30 July 2019
Received in revised form 28 September 2019
Accepted 29 September 2019
Available online 3 October 2019

Keywords:
Pillared-layer MOF
Photochemical cycloaddition
Structural transformation
Breathing MOF
Reticular chemistry

ABSTRACT

Single crystallinity of metal–organic frameworks (MOFs) enables the studies of their flexible behaviors with atomic precision. Here, we investigated the structural transformations triggered by photochemical cycloaddition and with temperature-dependent breathing in a series of pillared-layer MOF structures using a variety of pyrazolecarboxylate linkers for the layers and bipyridyl linkers as the pillars. The ethylenic double bonds from the pillars in close proximity undergo quantitative and seteroselective photochemical [2 + 2] cycloaddition upon UV irradiation, transforming the MOFs into structures with cyclobutane-based pillars. Furthermore, reversible breathing of the new pillared-layer MOF was evidenced by the 10.8% unit cell parameter change along *c* axis upon temperature change between 298 and 173 K. As revealed by single crystal X-ray diffraction, this transformation originates from the relative flattening of the wavy layers upon cooling. These two different types of characteristic structural transformations responding to inherent reactions and external stimuli happen at single crystalline state, providing a well-defined robust system with controlled flexibility.

1. Introduction

Compared with amorphous materials, materials in single crystal form allow researchers to study the detailed structural characteristics, and elucidate their relationships to specific properties. As one kind of crystalline porous materials, metal–organic frameworks (MOFs) are constructed by linking inorganic joints with organic linkers together in an absolute ordered manner [1–4]. MOFs have been demonstrated to be extremely functionalizable, flexible, and even adaptive without sacrificing their structural integrities [5–7]. Using single crystal X-ray technique, we are able to not only determine the atomic arrangements within the frameworks, but also take snapshots of structural transformations triggered by inherent reactions or external stimuli [8].

Among the various structural transformations of MOFs, we are particularly interested in exploring the delicate single-crystal to single-crystal transformations triggered by external light or temperature [9,10]. Photochemical reactions on the organic backbone of the MOFs have been frequently investigated to functionalize the porous materials. As one of the most studied photochemical reactions, classic [2 + 2] cycloaddition reactions of ethylenic double bonds in the linkers [11–14] have changed the dimensional connectivity of the MOFs [15–17], and produced polymers [18–20] or new organic molecules [21–23] with specific stereoselectivities. A prerequisite for the successful cycloaddition in MOF crystals is that the ethylenic double bonds need to be precisely arranged with the distance less than 4.2 Å between each other [24]. To keep olefin bonds in close proximity while still maintaining the high porosity of the materials, designing pillared-layer MOFs in which the cycloaddition reactions happen between the pillars, has been proved to be a viable strategy. Recently, significant progress has been made by smartly using pillar pair, rather than single pillar, for porous MOF construction and functionalizing them photochemically with exquisite control [25–29]. The MOFs after 100% photodimerization are still in single crystal form, providing a precise platform to study the materials' properties in gas separation [28] and sensing [30,31], etc.

On the other hand, structural transformations in MOFs could happen without any formation or dissociation of chemical bonds, but due to the intrinsic flexible nature of the frameworks. Breathing effect in MOFs could be stimulated by the change in temperature [32–34], mechanical pressure [35–37], and adsorption/desorption of guest molecules [38–40]. For example, reversible transformation with more than double increase in the unit cell volume is observed in the thermo-responsive MIL-53 [41]. Designing such responsive materials is requisite for fabricating temperature-

SPECIAL ISSUE: Emerging Investigators 2019

* Corresponding author.
E-mail address: qwli@fudan.edu.cn (Q. Li).

https://doi.org/10.1016/j.scib.2019.10.001
2095-9273/

triggered sensors and switches [42]. Various mechanisms to explain the temperature-dependent MOF structural transformation [43–45] have been examined, but more MOFs with definite structures before and after transformations are needed to understand MOFs' flexible behavior clearly.

Herein, we demonstrate two types of structural transformations—photochemical cycloaddition of the organic linkers and temperature-dependent breathing of the frameworks—in a series of pillared-layer MOF structures. By employing linkers featuring both pyrazolyl and carboxyl moieties as the organic edges for the construction of layers with square grids, and bipyridyl linkers as pillars, five new pillared-layer MOFs based on Zn_2 nodes, named FDM-61 to -65, were constructed. The open space within the porous single crystals could be finely regulated by adjusting the lengths of the layer linkers and the pillar linkers without altering the underlying topology. Particularly, FDM-62 and FDM-64 feature pairs of *trans*-1,2-bis(4-pyridyl)ethene linkers as the pillars, with distance between two ethylenic double bonds in the pair less than 3.93 Å. The pillar pairs undergo quantitative and seteroselective photochemical [2 + 2] cycloaddition upon UV irradiation, forming new MOFs with *regio-cis,trans,trans*-tetrakis(4-pyridyl) cyclobutane as the pillars. The structural transformation was confirmed by single crystal X-ray diffraction as well as ^{1}H NMR of the digested MOFs. What is more, after complete photodimerization of the pillars in FDM-64, the obtained FDM-66 single crystals demonstrate temperature-dependent breathing effect. The *c* parameter in FDM-66 shrinks from 34.62 to 30.87 Å when the crystals are cooled down from 298 to 173 K. The temperature-triggered 10.8% change in the unit cell length is reversible. A close investigation by crystallography revealed the relative flattening of the wavy layers in FDM-66 upon cooling, with the average dihedral angle of the two pyrazolates coordinating to the same Zn_2 node increased from 145.2° to 157.7°. The two types of structural transformations presented in the pillared-layer MOF system in a single-crystal to single-crystal manner demonstrate the MOFs' flexibility as responses to inherent reactions and external stimuli.

2. Experimental

2.1. Methods

All chemicals were purchased from commercial suppliers and used as received without further purifications. Fourier transform infrared spectroscopy (FT-IR) measurements were performed on a Nicolet iS10 FT-IR spectrometer with KBr pellets. Thermogravimetric analyses (TGA) of supercritical CO_2 activated samples were performed using a TA Instruments SDT-Q600 thermogravimetric analyzer with a heating rate of 10 °C min^{-1} under air atmosphere. Elemental analyses of C, H, and N were determined using automated vario EL III element analyzer. Elemental analyses of metals were obtained by using Teledyne Leeman Labs Prodigy high dispersion inductively coupled plasma optical emission spectrometer (ICP-OES). N_2 adsorption and desorption measurements were performed on a Quantachrome Autosorb-iQ_2 gas sorption analyzer, or a Micromeritics ASAP 2020 surface area and porosity analyzer at 77 K. Ultraviolet (UV) irradiation experiments were carried out by using six 8 W UV lamps (λ = 365 nm) as the irradiation source. Solution ^{1}H nuclear magnetic resonance (^{1}H NMR) spectra were obtained on a Bruker Avance III HD 400 spectrometer at 298 K. Powder X-ray diffraction (PXRD) was carried out using a Bruker AXS D8 Advance X-ray powder diffractometer operated at 1600 W power (40 kV, 40 mA) using Cu Kα radiation. The simulated PXRD patterns were calculated using Mercury 3.0 from the corresponding single-crystal structural data. Single crystal X-ray diffraction (SXRD) data was collected on a Bruker SMART Apex II single-crystal X-ray diffractometer equipped with a CCD area detector and operated at 50 kV, 30 mA to generate Mo Kα radiation (λ = 0.71073 Å), or a Bruker D8 Venture Metaljet diffractometer equipped with a photon II detector and operated at 70 kV, 2.85 mA to generate Ga Kα radiation (λ = 1.34138 Å). The crystallographic data for all structures were deposited in the Cambridge Structural Database (CSD), with the CCDC numbers 1943821–1943827. These data can be obtained free of charge from The Cambridge Crystallographic Data Centre via www.ccdc.cam.ac.uk/data_request/cif.

2.2. Synthesis of $[Zn_2(PyC)_2(BPy)]$ (FDM-61)

Single crystals of FDM-61 could be synthesized successfully within a relatively wide metal-to-linker ratio range, and similar crystalline qualities and yields are achieved. Typically, $Zn(NO_3)_2{\cdot}6H_2O$ (37.0 mg, 0.125 mmol), 4-pyrazolecarboxylic acid (H_2PyC, 8.4 mg, 0.075 mmol), and 4,4′-bipyridine (BPy, 7.8 mg, 0.05 mmol) were dissolved in a solution of 1.5 mL *N*,*N*-diethylformamide (DEF) and 0.5 mL water in a 4-mL vial. The vial was capped tightly and placed in an oven at 85 °C for 24 h. Colorless polyhedral crystals were collected and rinsed with *N*,*N*-dimethylformamide (DMF) for three times. Yield: 45% based on H_2PyC or 27% based on Zn (II). Elemental analysis for activated FDM-61 (solvent exchanged with EtOH nine times over three days, followed by supercritical CO_2 activation): Calc. (Found, %) for $[Zn_2(PyC)_2(BPy)]$ ($C_{18}H_{12}N_6O_4Zn_2$): C = 42.63 (39.31); H = 2.39 (3.50); N = 16.57 (15.13); Zn = 25.79 (24.76). FT-IR: (KBr, 4000–450 cm^{-1}): 3424(w), 1546 (vs), 1426(s), 1284(vs), 1221(w), 1175(w), 1048(s), 1005(s), 897 (w), 802(s), 729(w), 623(w), 606(w), 498(w).

2.3. Synthesis of $[Zn_{1.94}Cu_{0.06}(PyC)_2(BPE)]$ (FDM-62)

$Zn(NO_3)_2{\cdot}6H_2O$ (60.0 mg, 0.2 mmol), $Cu(NO_3)_2{\cdot}3H_2O$ (0.6 mg, 2.5 μmol), H_2PyC (22.4 mg, 0.2 mmol), and *trans*-1,2-bis(4-pyridyl)ethene (BPE, 18.4 mg, 0.1 mmol) were dissolved in a solution of 3.0 mL DEF, 3.0 mL *N*,*N*-dimethylacetamide (DMA), and 2.0 mL water in a 20-mL vial. The vial was capped tightly and placed in an oven at 85 °C for 24 h. Light blue block crystals were collected and rinsed with DMF for three times. Yield: 39% based on H_2PyC or 38% based on Zn(II). Elemental analysis for activated FDM-62 (solvent exchanged with EtOH nine times over three days, followed by supercritical CO_2 activation): Calc. (Found, %) for $[Zn_{1.94}Cu_{0.06}(PyC)_2(BPE)]$ ($C_{20}H_{14}N_6O_4Zn_{1.94}Cu_{0.06}$): C = 45.07 (41.84); H = 2.65 (3.54); N = 15.77 (14.84); Cu = 0.72 (0.75); Zn = 23.80 (24.27). FT-IR: (KBr, 4000–450 cm^{-1}): 3424(w), 1615 (vs), 1597(s), 1549(vs), 1434(s), 1375(w), 1282(vs), 1210(w), 1169(w), 1051(s), 1027(s), 1005(s), 890(w), 823(s), 796(s), 624 (w), 568(w), 553(w).

2.4. Synthesis of $[Zn_2(PyBC)_2(BPy)]$ (FDM-63)

$Zn(NO_3)_2{\cdot}6H_2O$ (15.0 mg, 0.05 mmol), 4-(1*H*-pyrazol-4-yl) benzoic acid (H_2PyBC, 9.4 mg, 0.05 mmol), and BPy (4.0 mg, 0.025 mmol) were dissolved in a solution of 1.5 mL DMF and 0.5 mL DMA in a 4-mL vial. The vial was capped tightly and placed in an oven at 85 °C for 24 h. Colorless polyhedral crystals were collected and rinsed with DMF for three times. Yield: 33% based on H_2PyBC or Zn(II). Elemental analysis for activated FDM-63 (solvent exchanged with EtOH nine times over three days, followed by supercritical CO_2 activation): Calc. (Found, %) for $[Zn_2(PyBC)_2(BPy)]$ ($C_{30}H_{20}N_6O_4Zn_2$): C = 54.65 (52.40); H = 3.06 (3.68); N = 12.75 (12.07); Zn = 19.83 (21.34). FT-IR: (KBr, 4000–450 cm^{-1}): 3425 (w), 1610(vs), 1534(s), 1504(w), 1404(vs), 1359(s), 1301(w), 1249(s), 1225(w), 1180(s), 1106(w), 1047(s), 1012(w), 953(s), 857(s), 809(w), 785(s), 708(w), 635(w), 570(w), 516 (w).

2.5. Synthesis of $[Zn_2(PyBC)_2(BPE)]$ (FDM-64)

$Zn(NO_3)_2{\cdot}6H_2O$ (15.0 mg, 0.05 mmol), H_2PyBC (9.4 mg, 0.05 mmol), and BPE (4.6 mg, 0.025 mmol) were dissolved in a solution of 1.5 mL DMF and 0.5 mL DMA in a 4-mL vial. The vial was capped tightly and placed in an oven at 85 °C for 24 h. Yellow plate crystals were collected and rinsed with DMF for three times. Yield: 37% based on H_2PyBC or Zn(II). Elemental analysis for activated FDM-64 (solvent exchanged with EtOH nine times over three days, followed by supercritical CO_2 activation): Calc. (Found, %) for $[Zn_2(PyBC)_2(BPE)]$ ($C_{32}H_{22}N_6O_4Zn_2$): C = 56.08 (53.25); H = 3.24 (3.89); N = 12.26 (11.54); Zn = 19.08 (19.11). FT-IR: (KBr, 4000–450 cm^{-1}): 3439(w), 1669(w), 1612(vs), 1555(w), 1501(w), 1426(w), 1384(vs), 1361(s), 1301(w), 1250(s), 1177(w), 1114(w), 1048(s), 1022(w), 955(w), 848(w), 782(w), 701(w), 553(w), 516(w).

2.6. Synthesis of $[Zn_2(PyC)_2(BPE){\cdot}(BPE)_{0.5}]$ (FDM-65)

$Zn(NO_3)_2{\cdot}6H_2O$ (30.0 mg, 0.1 mmol), H_2PyC (11.2 mg, 0.1 mmol), and BPE (9.1 mg, 0.05 mmol) were dissolved in a solution of 0.75 mL DMA, 0.75 mL ethanol, and 0.5 mL water in a 4-mL vial. The vial was capped tightly and placed in an oven at 100 °C for 24 h. Yellow plate crystals were collected and rinsed with DMF for three times. Yield: 58% based on H_2PyC or Zn(II). Elemental analysis for activated FDM-65 (solvent exchanged with CH_2Cl_2 nine times over three days, followed by heating at 60 °C under vacuum): Calc. (Found, %) for $[Zn_2(PyC)_2(BPE){\cdot}(BPE)_{0.5}]$ ($C_{26}H_{19}N_7O_4Zn_2$): C = 50.03 (48.25); H = 3.07 (3.30); N = 15.71 (15.62); Zn = 20.95 (20.78). FT-IR: (KBr, 4000–450 cm^{-1}): 3421 (w), 3122(w), 3078(w), 3048(w), 2474(w), 1952(w), 1702(w), 1615(vs), 1596(vs), 1548(vs), 1507(s), 1433(vs), 1418(vs), 1373 (s), 1282(vs), 1210(s), 1169(w), 1074(w), 1048(s), 1027(s), 1005 (s), 890(w), 841(s), 824(vs), 795(vs), 672(w), 626(w), 553(vs), 499(w), 475(w).

2.7. Water stability tests of FDM-62 and FDM-65

As-synthesized crystals of FDM-62 or FDM-65 were washed with DMF and deionized water, and then immersed in water (5 mg crystals per 1 mL water) in vials, and stood at ambient temperature. PXRD patterns of both samples were measured at certain time intervals. For the stability test of FDM-65 in boiling water, the washed crystals of FDM-65 were immersed in deionized water (5 mg crystals per 1 mL water) in a 25-mL round-bottom flask. The flask was then heated in oil bath at 100 °C for 7 d.

2.8. Photochemical cycloaddition in FDM-62 and FDM-64

Single crystals of FDM-62 or FDM-64 (~100 mg) were immersed in DMF solvent (8.0 mL) in a quartz reactor, respectively. Six UV lamps (365 nm, 8 W) were installed on top of the reactor with a fixed distance of ~12 cm between the light source and the crystals. During the UV irradiation, ~5 mg crystals were taken out at certain time intervals for further characterization, and the crystals remained in the reactor were shaken a bit to assure sufficient and uniform exposure to the light.

3. Results and discussion

3.1. Construction of the pillared-layer MOFs with paired pillars

Solvothermal reaction of $Zn(NO_3)_2{\cdot}6H_2O$, H_2PyC, and BPy in mixed solvents of DEF and H_2O at 85 °C gives single crystals of $[Zn_2(PyC)_2(BPy)]$ (FDM-61, Fig. 1a). Single crystal XRD revealed that FDM-61 crystallized in the orthorhombic *Pnnm* space group (Table S1 online), and was found to be a three-dimensional (3D) pillared-layer MOF structure. In each node, two Zn(II) ions are coordinated with four PyC linkers with NN from two pyrazolyl groups and O from two carboxyl groups. Connecting the nodes together with PyC linkers, two-dimensional layers with square

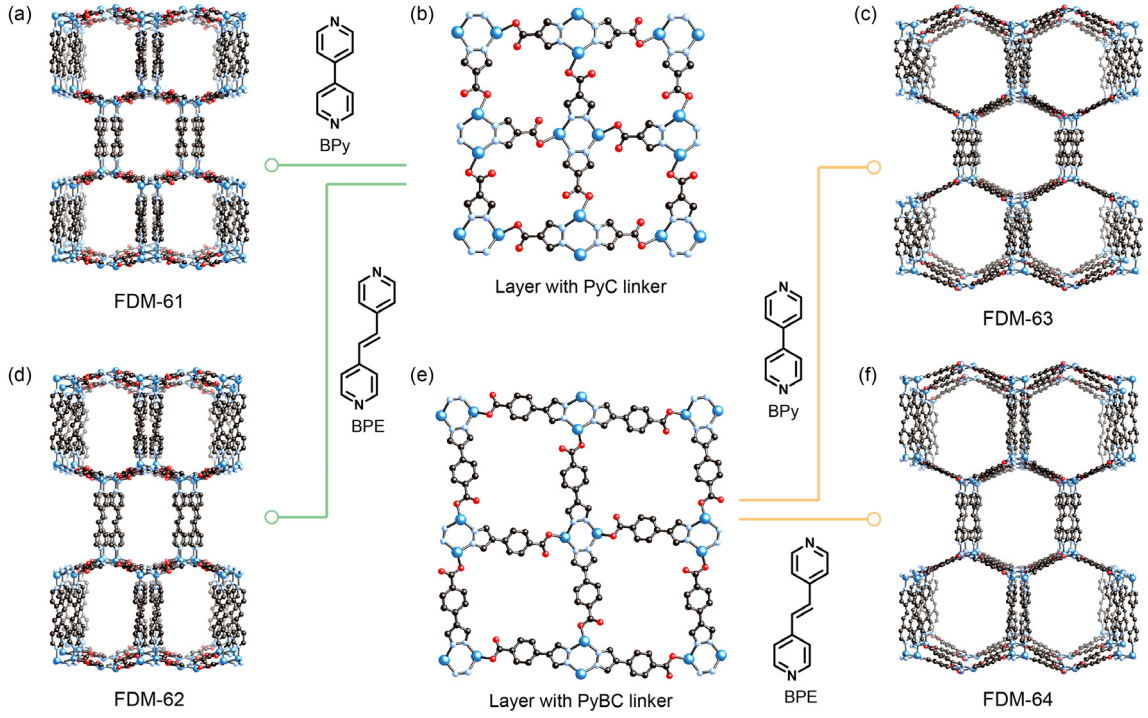

Fig. 1. (Color online) Single crystal structures of pillared-layer FDM-61 to FDM-64. FDM-61 (a) and FDM-62 (d) are constructed by connecting PyC-based layers (b) with BPy and BPE pillars, respectively. On the other hand, FDM-63 (c) and FDM-64 (f) are obtained by connecting PyBC-based layers (e) with BPy and BPE pillars, respectively.

grids were obtained (Fig. 1b). Furthermore, 3D pillared-layer FDM-61 was constructed by connecting Zn_2 nodes from adjacent layers with BPy pillars (Fig. 1a). The distance between the two Zn(II) in each node is only 3.59 Å, which makes the BPy pillars to be arranged in face-to-face pairs. The centers of two pairing BPy linkers are separated by ~3.80 Å, indicating the presence of π···π interaction between parallel pyridyl groups. Overall, the Zn(II) center has a pseudo-tetrahedral coordination geometry, and the BPy pairs are arranged in an alternating up/down manner along each layer. The resulting FDM-61 has a topology of **sqp** by considering the pillar pair as one edge, and features interconnected channels with size of ~10.0 Å × 4.8 Å.

By replacing the BPy with the longer BPE as pillars in the synthesis, single crystals of $[Zn_{1.94}Cu_{0.06}(PyC)_2(BPE)]$ (FDM-62) were synthesized (Fig. 1d). X-ray crystallographic analysis revealed the tetragonal $P4_2/mnm$ space group (Table S2 online). Isoreticular with pillared-layer FDM-61, FDM-62 is constructed by using PyC and Zn(II) for the layers, and BPE for the pillars. However, the interlayer distance of FDM-62 is 15.5 Å, a 2.4 Å increase compared with that of FDM-61 due to the longer BPE pillar. The pillar expansion also makes the pore size of FDM-62 being ~12.5 Å × 5.6 Å, as measured in the single crystal structure. The orientational disorder of BPE pillars was observed, which is attributed to the recognized pedal motion and the concomitant interconversion of two alternating BPE conformers [46,47]. The average distance between two ethylenic double bonds in the BPE pair is only 3.84 Å, providing opportunities for cycloaddition reactions between the two neighboring pillars.

It is worth mentioning that during the synthesis of FDM-62, trace amount of Cu(II) was added to the solution (feeding molar ratio of Zn(II) to Cu(II) is 80:1) to greatly improve the crystal quality of FDM-62 [48]. In the absence of Cu(II), we could still acquire FDM-62, but with poor single crystalline quality. Occasionally, other MOF structures as impurities were also observed. By introducing Cu(II) to the synthesis, high quality FDM-62 single crystals sufficient for single crystal X-ray diffraction studies were obtained. Furthermore, the use of Cu(II) avoids the impurity formation. As determined by ICP-OES, the ratio of Zn:Cu is 1.94:0.06 in FDM-62. When similar synthesis but with pure Cu(II) as metal source was performed, mixed phases of three different structures were obtained (see Supplementary data online for more details).

FDM-61 and FDM-62 demonstrate the capability of functionalizing the pillared-layer MOFs by modifying the pillar length and specific functional groups in the pillars. On the other hand, exercising the principles of reticular chemistry, we could also introduce different layer linkers to further modify the layers and the consequent MOF structures. Employing PyBC linkers, which is 4.3 Å longer than PyC, to constitute the layers for the pillared-layer MOFs (Fig. 1e), $[Zn_2(PyBC)_2(BPy)]$ (FDM-63, Fig. 1c) and $[Zn_2(PyBC)_2(BPE)]$ (FDM-64, Fig. 1f) were obtained (Tables S3 and S4 online). Both FDM-63 and FDM-64 are isostructural with FDM-61 and FDM-62. The square grid size in the layers of FDM-63 and FDM-64 is 13.7 Å, making enough room for both structures to be doubly interpenetrated. By measuring the single crystal structures, FDM-63 has a pore size of ~11.0 Å × 10.2 Å; while FDM-64 features 1D channel with ~12.0 Å × 11.7 Å in size (Fig. S1 online). In FDM-64, the ethylenic double bonds of paired BPE pillars show criss-cross arrangements with the average center-to-center distance of 3.93 Å.

The bulk purities of four new pillared-layer MOFs were confirmed by PXRD (Figs. S2–S5 online). Careful examination on the experimental and the simulated patterns suggests no other phases are generated in the one-pot mixed linker synthesis. Thermal stabilities of all structures were further investigated by TGA (Fig. S7 online). Compared to the non-interpenetrated FDM-61 and FDM-62, FDM-63 and FDM-64 with interpenetrated frameworks show relatively higher thermal stabilities. Specifically, FDM-63 and FDM-64 could be thermally stable up to 400 °C. Furthermore, the porosities of the MOFs were determined by N_2 adsorption isotherms. FDM-62 has a Brunauer-Emmett-Teller (BET) surface area of 146 $m^2 g^{-1}$, while other MOFs do not show meaningful N_2 uptake at 77 K (Fig. S8 online).

3.2. Paired vs. alternating pillar arrangement in FDM-62 and FDM-65

In FDM-61 to -64 with the same topology, the two pillar linkers connecting to the same Zn_2 node are on the same side of the layer, and inter-pillar interactions are evident by their close distance between each other (Fig. 2a). At the same time, by adjusting the reaction condition, we managed to obtain a topologically different pillared-layer MOF, named FDM-65 $[Zn_2(PyC)_2(BPE)\cdot(BPE)_{0.5}]$ (Figs. S6 and S7 online). The two types of organic linkers adopted in FDM-65 (PyC and BPE) are the same as those in FDM-62. X-ray crystallographic analysis revealed that FDM-65 crystallized in orthorhombic *Pccn* space group (Table S5 online). Similar layer structure with FDM-62 is observed in FDM-65; however, the arrangement of the pillars is different in these two MOF structures. In FDM-65, the two pillars connecting to the same Zn_2 node are arranged on the opposite sides of the layer (Fig. 2b). As a result, no pairing of the pillars is observed in FDM-65, and the topology of the overall network is **pcu** instead. In addition to serving as the pillars for the pillared-layer structure, BPE is also located in the pores as the guest molecules with host-guest π···π interaction.

Furthermore, the structure of FDM-65 is doubly interpenetrated, while FDM-62 is non-interpenetrated. Considering the same square grids in the layers for both MOFs, we believe that different arrangement of the pillars is responsible for the interpenetration in FDM-65. Using PyC as the layer linker, the opening of the square grid is only ~4.0 Å in diameter. This opening is possible for one BPE linker to be inserted into, but not possible for a pair of BPE linkers (with a diameter of ~7.2 Å). In other words, FDM-62 has paired pillars, thus interpenetration is forbidden. In the case of FDM-65, however, the tendency of forming pillar pairs is suppressed by the alternative interactions between the pillars and the free BPE molecules in the pores. As a result, the two pillars are arranged on the opposite sides of the layer. Indeed, the free BPE molecules are perfectly sandwiched between the pillars from two interpenetrating nets in FDM-65 (Fig. S9 online), with an average π···π distance of 3.43 Å.

The restricted pore space due to the interpenetration and the precisely sandwiched BPE guests in the pores have contributed to the significantly improved chemical stability of FDM-65. FDM-65 retains its framework integrity after the crystals were immersed in deionized water for 10 months, as evidenced by the almost unchanged PXRD patterns (Fig. 2c). Moreover, structure of FDM-65 is maintained after the crystals were kept in boiling water for 7 d. In contrast, after water treatment for 1 h at ambient temperature, crystals of FDM-62 lose the overall crystallinity with obvious PXRD pattern change and dramatic peak intensity weakening (Fig. 2d). A close investigation on the FDM-65 crystal structure revealed that the Zn(II)-carboxylate coordination, which is the least stable linkage when immersed in water, is closely surrounded by pillars from the second net and BPE guest molecules. This environment has prevented the formation of water clusters near the metal centers in FDM-65, contributing to higher water stability.

3.3. Photochemical cycloaddition in FDM-62 and FDM-64

In both FDM-62 and FDM-64, the paired BPE linkers show face-to-face arrangement with the distance between two ethylenic double bonds less than 4.2 Å (3.84 Å for FDM-62 and 3.93 Å for FDM-64), meeting the Schmidt's criteria for photochemical [2 + 2] cycloaddition reaction [24]. When the cycloaddition happens in

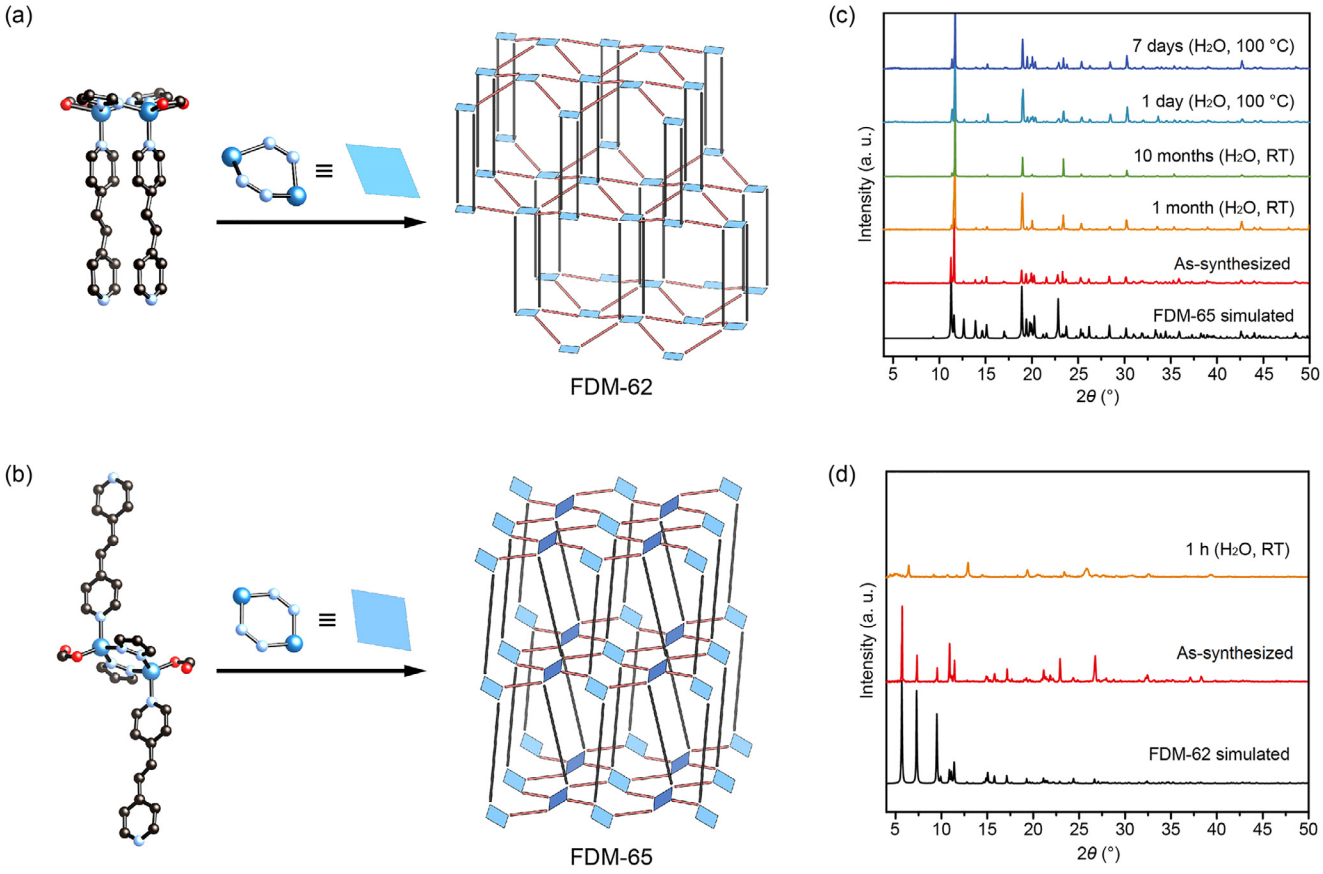

Fig. 2. (Color online) Structural and chemical stability comparisons between FDM-62 and FDM-65. (a) Paired BPE pillars are on the same side of the layer to form **sqp**-type FDM-62. (b) BPE pillars are arranged on the opposite sides of the layer to form **pcu**-type FDM-65. Their water stability difference is evidenced by the PXRD patterns of FDM-65 (c) and FDM-62 (d) in deionized water for different time intervals.

the MOF crystals, it further imposes stereoselectivity to the cyclobutane product. To elucidate the photochemical reactivity of the two MOFs in single crystal form, single crystals of FDM-62 and FDM-64 in DMF were irradiated under UV light (365 nm) for 6 h. ^{1}H NMR spectra of the DCl digested MOF samples (Fig. S10 online) were taken every 30 min to monitor the photodimerization of the paired BPE linkers. Specifically, the ^{1}H NMR spectra showed complete disappearance of the chemical shifts from the olefin protons (7.87 ppm for FDM-62 and 8.07 ppm for FDM-64), and appearance of the cyclobutane proton signals of the resulted stereoselective *regio-cis,trans,trans*-tetrakis(4-pyridyl)cyclobutane (*rctt*-tpcb) product (5.43 and 5.44 ppm, respectively). Note that ethylenic double bonds of BPE linkers may arrange in a criss-cross mode, they could undergo pedal motion and switch to parallel conformation prior to the [2 + 2] cycloaddition reaction, and make *rctt*-tpcb the only stereoselective product [19,47,49]. In addition, the signals of pyridyl protons shifted from 8.76, 8.24 to 8.65, 7.99 ppm in the digested FDM-62, and from 8.91, 8.35 to 8.72, 8.08 ppm in the digested FDM-64, respectively. The ratios between the BPE linker and the resulted *rctt*-tpcb product in two MOF crystals were calculated based on the peak integration in ^{1}H NMR spectra, and they revealed progressive conversion from BPE to *rctt*-tpcb upon UV irradiation (Fig. 3a and b). Considering one *rctt*-tpcb linker is produced by every two BPE linkers, the conversion reaches 50% when the molar ratio between BPE and *rctt*-tpcb reaches 2:1 in the system. This point was met upon UV exposure for ~60 min for FDM-62 (~70 min for FDM-64). Close to 100% photodimerization yields were achieved after more than 6 h for FDM-62, and 5 h for FDM-64, respectively.

The structural transformation by photochemical cycloaddition was further confirmed by the PXRD patterns of the MOFs after they were irradiated for different time intervals. For example, in FDM-62, a noticeable new peak appeared at 2θ of 6.4° after it was exposed to UV light for ~1 h, and the peak intensity increased gradually along time (Fig. 3c). On the other hand, the intensities of 2θ at 5.7°, 10.8°, 11.0°, and 14.8°, corresponding to (0 0 2), (1 0 3), (1 1 2), and (1 1 4) reflections of FDM-62, decreased along the irradiation time. In the case of FDM-64, the PXRD change was subtle, but several new peaks with relatively weak intensity appeared at 9.1°, 13.8°, and 17.2° (Fig. 3d). Together with ^{1}H NMR results, PXRD clearly support that BPE pillar linkers in FDM-62 and FDM-64 are converted into *rctt*-tpcb quantitatively upon UV irradiation, accompanied by the unit cell parameters change during the photodimerization.

To gain direct insights into the structural details of the MOFs after cycloaddition, we successfully obtained the single crystal structure of the fully photodimerized product based on FDM-64, termed FDM-66 (Fig. 3e). The formation of *rctt*-tpcb gave rise to the change of space group from *Pnna* for FDM-64 to $P2_1/n$ for FDM-66. As expected, FDM-66 shows *rctt*-tpcb as pillars in the structure, with the C–C bond lengths in the cyclobutane being 1.58–1.72 Å at 298 K. During the single-crystal to single-crystal transformation, the unit cell parameters keep almost constant, despite the space group changes to lower symmetry (Table 1). This also explains the subtle change in the PXRD at room temperature upon irradiation for FDM-64 (Fig. 3d). Overall, single crystallinity is maintained during the cycloaddition, demonstrating the dynamics and reactivity of the pillar linkers triggered by light in the robust framework.

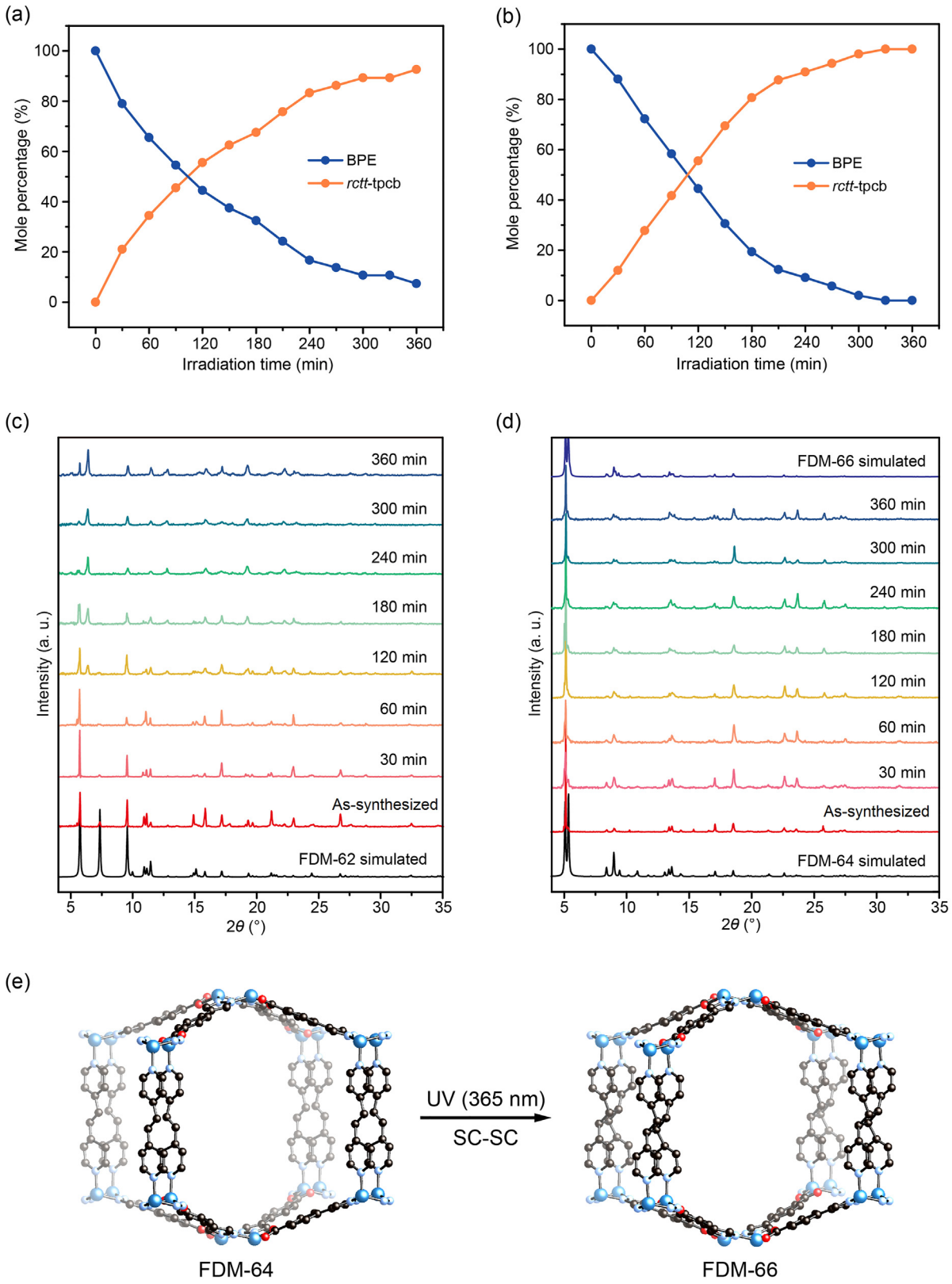

Fig. 3. (Color online) Photochemical cycloaddition reactions in FDM-62 and FDM-64. (a, b) Mole percentage changes of the unreacted BPE pillars and the *rctt*-tpcb products in FDM-62 and FDM-64 crystals during the photodimerization process, respectively. (c, d) PXRD patterns of FDM-62 and FDM-64 under UV irradiation for different time intervals, respectively. (e) Single-crystal to single-crystal transformation from FDM-64 to FDM-66 by photochemical [2 + 2] cycloaddition reaction.

Table 1
Structural parameters of FDM-64, FDM-66-298K, and FDM-66-173K.

MOFs	Unit cell parameters		Volume (Å^3)	Pillar length (Å)[a]	θ (°)[b]
	a, *b*, *c* (Å)	β (°)			
FDM-64	18.57, 18.74, 34.58	90.00	12,036	13.44	145.0
FDM-66-298K	18.40, 18.90, 34.62	90.92	12,040	13.40	145.2
FDM-66-173K	18.97, 19.45, 30.87	91.96	11,384	13.29	157.7

[a] Average distance of Zn···BPE···Zn or Zn···*rctt*-tpcb···Zn.
[b] Dihedral angle of the two pyrazolates coordinating to the same Zn_2 node.

3.4. Temperature-dependent breathing in FDM-66

We found that FDM-66 features different unit cell parameters when the single crystal X-ray diffraction data is collected at 173 or at 298 K (Tables S6 and S7 online). Both structures, named FDM-66-173 K and FDM-66-298 K in this context, have the same $P2_1/n$ space group and the same atomic connectivity, but with different cell parameters (Table 1). Particularly, a significant decrease in *c* from 34.62 to 30.87 Å was observed when the crystal is cooled down from 298 to 173 K (Fig. 4a). This represents a 10.8% change along the *c* direction. On the other hand, ~3% increase in *a* and *b* directions was measured, and the total unit cell volume shrinks about 5.4%. This structural transformation is reversible, as evidenced by the full recovery of the original unit cell when the crystals were warmed up to room temperature.

A careful comparison between FDM-66-173K and FDM-66-298K revealed that the layers in FDM-66-298K are wavier than those in FDM-66-173K. The average dihedral angles between the two pyrazolates coordinating to the same Zn_2 node are 145.2° and 157.7° for FDM-66-298K and FDM-66-173K, respectively (Fig. 4b). Similarly, the average dihedral angle between the two carboxylates connecting to the same node also increases from 142.6° to 150.2° when the crystal was cooled down to 173 K. The dihedral angle increase has significantly flattened the layers, thus a reduction on the *c* parameter was observed.

We sought to understand the origin of the bistable structural breathing effect triggered by the temperature change. A careful analysis on the *rctt*-tpcb pillars suggests no conformational change on the pillar linker, and the pillar length remains almost constant (13.3–13.4 Å, measured by the distance between two Zn(II) from neighboring layers). In addition, overlapping the structures of FDM-66-298K and FDM-66-173K (Fig. S11 online) shows the coordination environment around the pseudo-tetrahedral Zn(II) remains almost unchanged, with the average bond angle change around pyrazolyl N–Zn(II)–pyrazolyl N being less than 1.7° (Fig. S12 and Table S8 online). This value is significantly smaller than the 12.5° change in the dihedral angle between the two pyrazolates. Thus, we conclude that the flexible nature of FDM-66 originates from the PyBC layer linker. The subtle change on the bond angle and coplanarity in the PyBC linker has been amplified into the moderate unit cell parameter change in the crystal. Similar vibration behaviors of linker act as a "knee" have been reported [50,51]. Previously, mechanisms of thermo-responsive MOFs were explained by linker rotation [43], side chain motion [44], dispersive

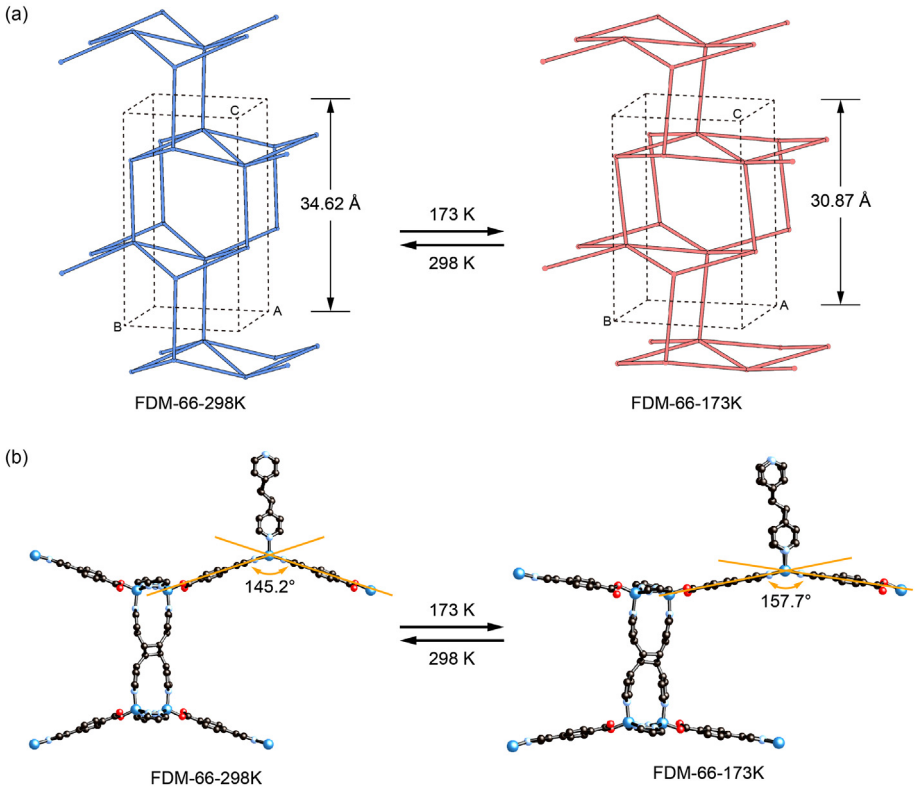

Fig. 4. (Color online) Temperature-dependent breathing in FDM-66. (a) Reversible transformation between FDM-66-298K and FDM-66-173K is evident by the *c* parameter change in the unit cell. (b) Average dihedral angle of the two pyrazolates coordinating to the same Zn_2 node increases from FDM-66-298K to FDM-66-173K.

interactions and entropy stabilization [41,45], or host-guest and guest-guest interactions [51,52]. In our work, the crystals of FDM-66 for structural determination at different temperatures were obtained with DMF solvent in the pores. As no linker rotation and side chain is involved in FDM-66, we believe the reversible breathing of the network without the adsorption/desorption of any guest is probably induced by the $\pi\cdots\pi$ interactions of PyBC linkers, the MOF host-solvent guest interactions, and/or guest molecules rearrangement.

4. Conclusions

In summary, by adopting the same pillared-layer structure topology, four new MOFs (FDM-61 to -64) were constructed using layer linkers and pillar linkers with varied lengths and functional groups. With the ethylenic double bonds in the pillars of the structures, FDM-62 and FDM-64 could convert to new MOF structures with cyclobutane-based pillars by classic photochemical [2 + 2] cycloaddition reactions, demonstrating the capability of structural transformation in single crystal form. The paired arrangement of olefin-based pillars is necessary for the photodimerization. In contrast, pillared-layer structure FDM-65 with higher water stability could not undergo cylcoaddition due to larger inter-pillar distance. Furthermore, breathing behavior triggered by temperature change was demonstrated in the single crystals of cyclobutane-based FDM-66, with 10.8% cell parameter change along *c* axis. The work presented here affords a great platform for researchers to study the elaborate structural transformations in porous crystalline materials. In the future, we will explore the potential applications in sensing of the materials with temperature-dependent breathing.

Conflict of interest

The authors declare that they have no conflict of interest.

Acknowledgments

This work was supported by the National Natural Science Foundation of China (21571037, 21733003, and 21961132003), the National Key Research and Development Program of China (2018YFA0209400), the National Top-Notch Talent Program, the Science & Technology Commission of Shanghai Municipality (16520710100, 17JC1400100), and the China Postdoctoral Science Foundation (2018M632003).

Author contributions

Qiaowei Li conceived and designed the research; Qingqing Pang, Binbin Tu, and Lingyi Yang performed the research; Qingqing Pang and Qiaowei Li wrote the manuscript with contributions from all authors. All authors discussed the results and commented on the manuscript.

Appendix A. Supplementary data

Supplementary data to this article can be found online at https://doi.org/10.1016/j.scib.2019.10.001.

References

[1] Yaghi OM, O'Keeffe M, Ockwig NW, et al. Reticular synthesis and the design of new materials. Nature 2003;423:705–14.
[2] Kitagawa S, Kitaura R, Noro SI. Functional porous coordination polymers. Angew Chem Int Ed 2004;43:2334–75.
[3] Férey G. Hybrid porous solids: past, present, future. Chem Soc Rev 2008;37:191–214.
[4] Furukawa H, Cordova KE, O'Keeffe M, et al. The chemistry and applications of metal–organic frameworks. Science 2013;341:1230444.
[5] Cohen SM. Postsynthetic methods for the functionalization of metal–organic frameworks. Chem Rev 2012;112:970–1000.
[6] Schneemann A, Bon V, Schwedler I, et al. Flexible metal–organic frameworks. Chem Soc Rev 2014;43:6062–96.
[7] Morris RE, Brammer L. Coordination change, lability and hemilability in metal–organic frameworks. Chem Soc Rev 2017;46:5444–62.
[8] Zhang JP, Liao PQ, Zhou HL, et al. Single-crystal X-ray diffraction studies on structural transformations of porous coordination polymers. Chem Soc Rev 2014;43:5789–814.
[9] He WW, Li SL, Lan YQ. Liquid-free single-crystal to single-crystal transformations in coordination polymers. Inorg Chem Front 2018;5:279–300.
[10] Kole GK, Vittal JJ. Solid-state reactivity and structural transformations involving coordination polymers. Chem Soc Rev 2013;42:1755–75.
[11] Hao J, Xu X, Fei H, et al. Functionalization of metal–organic frameworks for photoactive materials. Adv Mater 2018;30:1705634.
[12] Huang SL, Hor TSA, Jin GX. Photodriven single-crystal-to-single-crystal transformation. Coord Chem Rev 2017;346:112–22.
[13] Wang XY, Wang ZM, Gao S. A pillared layer MOF with anion-tunable magnetic properties and photochemical [2 + 2] cycloaddition. Chem Commun 2007:1127–9.
[14] Eubank JF, Kravtsov VC, Eddaoudi M. Synthesis of organic photodimeric cage molecules based on cycloaddition via metal-ligand directed assembly. J Am Chem Soc 2007;129:5820–1.
[15] Medishetty R, Koh LL, Kole GK, et al. Solid-state structural transformations from 2D interdigitated layers to 3D interpenetrated structures. Angew Chem Int Ed 2011;50:10949–52.
[16] Medishetty R, Tandiana R, Koh LL, et al. Assembly of 3D coordination polymers from 2D sheets by [2+2] cycloaddition reaction. Chem Eur J 2014;20:1231–6.
[17] Hu FL, Shi YX, Chen HH, et al. A Zn(II) coordination polymer and its photocycloaddition product: syntheses, structures, selective luminescence sensing of iron(III) ions and selective absorption of dyes. Dalton Trans 2015;44:18795–803.
[18] Park IH, Chanthapally A, Zhang Z, et al. Metal–organic organopolymeric hybrid framework by reversible [2+2] cycloaddition reaction. Angew Chem Int Ed 2014;53:414–9.
[19] Park IH, Medishetty R, Lee HH, et al. Formation of a syndiotactic organic polymer inside a MOF by a [2+2] photo-polymerization reaction. Angew Chem Int Ed 2015;54:7313–7.
[20] Medishetty R, Park IH, Lee SS, et al. Solid-state polymerisation via [2+2] cycloaddition reaction involving coordination polymers. Chem Commun 2016;52:3989–4001.
[21] Liu D, Ren ZG, Li HX, et al. Single-crystal-to-single-crystal transformations of two three-dimensional coordination polymers through regioselective [2+2] photodimerization reactions. Angew Chem Int Ed 2010;49:4767–70.
[22] Liu D, Wang HF, Abrahams BF, et al. Single-crystal-to-single-crystal transformation of a two-dimensional coordination polymer through highly selective [2+2] photodimerization of a conjugated dialkene. Chem Commun 2014;50:3173–5.
[23] Chen JM, Zhou QK, Hou YX, et al. Single-crystal-to-single-crystal conversions of two metal-mediated photoreactive coordination polymers based on stereoselective [2 + 2] photocycloaddition reactions. CrystEngComm 2017;19:6778–86.
[24] Schmidt GMJ. Photodimerization in the solid state. Pure Appl Chem 1971;27:647–78.
[25] Mir MH, Koh LL, Tan GK, et al. Single-crystal to single-crystal photochemical structural transformations of interpenetrated 3D coordination polymers by [2 +2] cycloaddition reactions. Angew Chem Int Ed 2010;49:390–3.
[26] Park IH, Ju H, Kim K, et al. Isomerism in double-pillared-layer coordination polymers – structures and photoreactivity. IUCrJ 2018;5:182–9.
[27] Hu FL, Wang SL, Lang JP, et al. *In-situ* X-ray diffraction snapshotting: determination of the kinetics of a photodimerization within a single crystal. Sci Rep 2014;4:6815.
[28] Foo ML, Matsuda R, Hijikata Y, et al. An adsorbate discriminatory gate effect in a flexible porous coordination polymer for selective adsorption of CO_2 over C_2H_2. J Am Chem Soc 2016;138:3022–30.
[29] Park IH, Lee E, Lee SS, et al. Chemical patterning in single crystals of metal–organic frameworks by [2+2] cycloaddition reaction. Angew Chem Int Ed 2019. https://doi.org/10.1002/anie.201904834.
[30] Li NY, Liu D, Abrahams BF, et al. Covalent switching, involving divinylbenzene ligands within 3D coordination polymers, indicated by changes in fluorescence. Chem Commun 2018;54:5831–4.
[31] Park IH, Medishetty R, Kim JY, et al. Distortional supramolecular isomers of polyrotaxane coordination polymers: photoreactivity and sensing of nitro compounds. Angew Chem Int Ed 2014;53:5591–5.
[32] Zhang JP, Lin YY, Zhang WX, et al. Temperature- or guest-induced drastic single-crystal-to-single-crystal transformations of a nanoporous coordination polymer. J Am Chem Soc 2005;127:14162–3.
[33] Wang XF, Wang Y, Zhang YB, et al. Layer-by-layer evolution and a hysteretic single-crystal to single-crystal transformation cycle of a flexible pillared-layer open framework. Chem Commun 2012;48:133–5.
[34] Collings IE, Cairns AB, Thompson AL, et al. Homologous critical behavior in the molecular frameworks $Zn(CN)_2$ and $Cd(imidazolate)_2$. J Am Chem Soc 2013;135:7610–20.

[35] Yot PG, Ma Q, Haines J, et al. Large breathing of the MOF MIL-47(V^{IV}) under mechanical pressure: a joint experimental-modelling exploration. Chem Sci 2012;3:1100–4.
[36] Beurroies I, Boulhout M, Llewellyn PL, et al. Using pressure to provoke the structural transition of metal–organic frameworks. Angew Chem Int Ed 2010;49:7526–9.
[37] Rodriguez J, Beurroies I, Loiseau T, et al. The direct heat measurement of mechanical energy storage metal–organic frameworks. Angew Chem Int Ed 2015;54:4626–30.
[38] Mason JA, Oktawiec J, Taylor MK, et al. Methane storage in flexible metal–organic frameworks with intrinsic thermal management. Nature 2015;527:357–61.
[39] Henke S, Schneemann A, Wütscher A, et al. Directing the breathing behavior of pillared-layered metal–organic frameworks via a systematic library of functionalized linkers bearing flexible substituents. J Am Chem Soc 2012;134:9464–74.
[40] Zhou DD, Liu ZJ, He CT, et al. Controlling the flexibility and single-crystal to single-crystal interpenetration reconstitution of metal–organic frameworks. Chem Commun 2015;51:12665–8.
[41] Liu Y, Her JH, Dailly A, et al. Reversible structural transition in MIL-53 with large temperature hysteresis. J Am Chem Soc 2008;130:11813–8.
[42] Wieme J, Lejaeghere K, Kresse G, et al. Tuning the balance between dispersion and entropy to design temperature-responsive flexible metal–organic frameworks. Nat Commun 2018;9:4899.
[43] Wharmby MT, Henke S, Bennett TD, et al. Extreme flexibility in a zeolitic imidazolate framework: porous to dense phase transition in desolvated ZIF-4. Angew Chem Int Ed 2015;54:6447–51.
[44] Henke S, Schneemann A, Fischer RA. Massive anisotropic thermal expansion and thermo-responsive breathing in metal–organic frameworks modulated by linker functionalization. Adv Funct Mater 2013;23:5990–6.
[45] Walker AM, Civalleri B, Slater B, et al. Flexibility in a metal–organic framework material controlled by weak dispersion forces: the bistability of MIL-53(Al). Angew Chem Int Ed 2010;49:7501–3.
[46] Harada J, Ogawa K. Invisible but common motion in organic crystals: a pedal motion in stilbenes and azobenzenes. J Am Chem Soc 2001;123:10884–8.
[47] Harada J, Ogawa K. Pedal motion in crystals. Chem Soc Rev 2009;38:2244–52.
[48] Yang H, Wang F, Kang Y, et al. Chiral assembly of dodecahedral cavities into porous metal–organic frameworks. Chem Commun 2012;48:9424–6.
[49] Chu Q, Swenson DC, MacGillivray LR. A single-crystal-to-single-crystal transformation mediated by argentophilic forces converts a finite metal complex into an infinite coordination network. Angew Chem Int Ed 2005;44:3569–72.
[50] Serre C, Mellot-Draznieks C, Surblé S, et al. Role of solvent-host interactions that lead to very large swelling of hybrid frameworks. Science 2007;315:1828–31.
[51] Wei YS, Chen KJ, Liao PQ, et al. Turning on the flexibility of isoreticular porous coordination frameworks for drastically tunable framework breathing and thermal expansion. Chem Sci 2013;4:1539–46.
[52] Zhou HL, Lin RB, He CT, et al. Direct visualization of a guest-triggered crystal deformation based on a flexible ultramicroporous framework. Nat Commun 2013;4:2534.

Qingqing Pang received her B.Eng. degree in 2012 from Jiangnan University and her Ph.D in 2017 from Fudan University under the direction of Prof. Qiaowei Li. She is currently a postdoctoral fellow in the Department of Chemistry, Fudan University with Prof. Qiaowei Li. Her current research is focusing on the synthesis of pillared-layer metal–organic frameworks and their photochemical properties study.

Qiaowei Li is currently a Professor of Chemistry at Fudan University, China. He received his B.S. degree in Applied Chemistry (2004) from University of Science & Technology of China, M.S. degree in Chemistry from University of Michigan (2006), and Ph.D. degree in Chemistry from University of California, Los Angeles (2010). His current research interests include the reticular chemistry of multicomponent metal–organic frameworks and ordered vacancies in porous crystals.